Large-scale poloidal magnetic field dynamo leads to powerful jets in GRMHD simulations of black hole accretion with toroidal field

M. Liska,[1]⋆ A. Tchekhovskoy[2,3] and E. Quataert [3]

[1]*Anton Pannekoek Institute for Astronomy, University of Amsterdam, Science Park 904, NL-1098 XH Amsterdam, the Netherlands*
[2]*Center for Interdisciplinary Exploration and Research in Astrophysics (CIERA), Physics and Astronomy, Northwestern University, Evanston, IL 60208, USA*
[3]*Departments of Astronomy and Physics, Theoretical Astrophysics Center, University of California Berkeley, Berkeley, CA 94720-3411, USA*

ABSTRACT

Accreting black holes (BHs) launch relativistic collimated jets, across many decades in luminosity and mass, suggesting the jet launching mechanism is universal, robust, and scale-free. Theoretical models and general relativistic magnetohydrodynamic (GRMHD) simulations indicate that the key jet-making ingredient is large-scale poloidal magnetic flux. However, its origin is uncertain, and it is unknown if it can be generated *in situ* or dragged inward from the ambient medium. Here, we use the GPU-accelerated GRMHD code H-AMR to study global 3D BH accretion at unusually high resolutions more typical of local shearing box simulations. We demonstrate that turbulence in a radially extended accretion disc can generate large-scale poloidal magnetic flux *in situ*, even when starting from a purely toroidal magnetic field. The flux accumulates around the BH till it becomes dynamically important, leads to a magnetically arrested disc (MAD), and launches relativistic jets that are more powerful than the accretion flow. The jet power exceeds that of previous GRMHD toroidal field simulations by a factor of 10 000. The jets do not show significant kink or pinch instabilities, accelerate to $\gamma \sim 10$ over three decades in distance, and follow a collimation profile similar to the observed M87 jet.

Key words: accretion, accretion discs – black hole physics – MHD – methods: numerical – galaxies: jets.

1 INTRODUCTION

BHs can launch relativistic jets by converting BH spin energy into Poynting flux (Blandford & Znajek 1977). The ratio of jet and accretion powers, or jet efficiency, is maximum when the BH is both rapidly spinning and has accumulated a substantial amount of large-scale poloidal (i.e. confined to a meridional, $R - z$ plane) magnetic flux (see e.g. Komissarov 2001; Tchekhovskoy, Narayan & McKinney 2010). Given enough poloidal magnetic flux, a magnetically arrested disc (MAD) can form (e.g. Narayan, Igumenshchev & Abramowicz 2003), with jet efficiency exceeding 100 per cent for thick (Tchekhovskoy, Narayan & McKinney 2011; McKinney, Tchekhovskoy & Blandford 2012; Tchekhovskoy & McKinney 2012) and reaching 50 per cent for thin discs (with an aspect ratio $h/r = 0.03$; Liska et al. 2019b).

One way of obtaining the large-scale poloidal magnetic flux near the BH is advecting it from large radii. While thick discs can do this over short distances (as confirmed by 3D GRMHD simulations, e.g. Hawley & Krolik 2006; Tchekhovskoy et al. 2011), it is unclear

whether they can do this over 5–6 orders of magnitude in distance, from the ambient medium all the way down to the BH. This is particularly uncertain given that in many systems the accretion discs at large radii are expected to cool radiatively and become thin. In such discs the poloidal magnetic flux may diffuse out faster than it can be advected inwards (Lubow, Papaloizou & Pringle 1994; however, see Rothstein & Lovelace 2008; Guilet & Ogilvie 2012, 2013).

Large-scale poloidal magnetic flux on the BH can also form *in situ* through a turbulent dynamo (Brandenburg et al. 1995) powered by the magnetorotational instability (MRI, see Balbus & Hawley 1991). Local shearing box studies found that the dynamo can produce radial and toroidal magnetic fluxes on the scale of the box (e.g. Brandenburg et al. 1995; Stone et al. 1996; Lesur & Ogilvie 2008; Davis, Stone & Pessah 2010; Simon, Beckwith & Armitage 2012; Shi, Stone & Huang 2016; Salvesen et al. 2016a; Ryan et al. 2017). However, persistent jets lasting an accretion time require poloidal magnetic flux on a much larger scale. Additionally, the often used quasi-periodic boundary conditions in the horizontal direction imply that the net vertical magnetic flux through the box cannot change in time: in fact, it is a crucial externally imposed parameter. Shearing box simulations without net flux do not appear to generate poloidal

⋆ E-mail: matthewliska92@gmail.com

magnetic flux that affects the turbulence in the same way the net flux does (Pessah, Chan & Psaltis 2007; Bai & Stone 2013; Bhat, Ebrahimi & Blackman 2016; Salvesen et al. 2016a,b).

Free from these limitations, global GRMHD simulations are particularly attractive for studying the formation of large-scale poloidal magnetic flux and the associated jets and outflows. Most global simulations have focused on the initial seed poloidal magnetic flux, in the form of one or several poloidal magnetic field loops; and those show no signs of a large-scale poloidal magnetic flux dynamo (e.g. Hawley & Krolik 2006; McKinney 2006; Shafee et al. 2008; Noble, Krolik & Hawley 2009; Penna et al. 2010; Narayan et al. 2012). Beckwith, Hawley & Krolik (2008) found that jets formed only for initial conditions with net poloidal magnetic flux, and no jets formed for a purely toroidal initial magnetic flux. For a similar toroidal magnetic field initial condition, but for a larger initial torus, McKinney et al. (2012) found short-lived jets with duration $\lesssim 12 M_{\rm BH}/(10^8 M_\odot)$ days and a low duty cycle, ~ 2 per cent, where $M_{\rm BH}$ is BH mass. Their low time-average efficiency, $\lesssim 0.01$ per cent, implied that such weak jets would disrupt easily through the kink instability (Bromberg & Tchekhovskoy 2016; Tchekhovskoy & Bromberg 2016). This low efficiency also appears insufficient to account for feedback from AGN jets on kiloparsec scales (e.g. Fabian 2012) and for the substantial jet power inferred in AGN jets (see, e.g. Prieto et al. 2016 for M87, Nemmen & Tchekhovskoy 2015 for low-luminosity AGN, and Ghisellini et al. 2014 for blazars). Thus, there appears to be a serious mismatch between theory and observations due to the inability of GRMHD simulations to generate sufficient large-scale poloidal magnetic flux starting without one initially.

Yet, toroidal magnetic flux is a natural starting point for accretion discs in various contexts. In compact object mergers, the orbital shear is expected to produce a toroidally-dominated magnetic field geometry. In X-ray binaries, the stream overflowing the Roche lobe (or wind from the companion star) would stretch out in the toroidal and radial directions as it feeds the outer disc, and the disc shear would then substantially amplify the toroidal component. Similarly, the tidal debris stream feeding the supermassive BH during a tidal disruption event (TDE) is also expected to lead to a toroidally dominated magnetic field. While AGN appear to have more than sufficient large-scale magnetic flux in the interstellar medium, it is unclear whether their thin accretion discs can drag it to the BH. Thus, it is important to understand whether accretion discs can produce large-scale poloidal magnetic flux on their own.

This motivates our study of BH accretion seeded with purely a toroidal magnetic flux. In Section 2 we describe the numerical setup, in Section 3 we present our results, and in Section 4 we conclude.

2 NUMERICAL APPROACH AND PROBLEM SETUP

We use the H-AMR code (Liska et al. 2018, 2019a) that evolves the GRMHD equations of motion (Gammie, McKinney & Tóth 2003) on a spherical polar–like grid in Kerr-Schild coordinates, using PPM spatial reconstruction (Colella & Woodward 1984) and second-order time-stepping. H-AMR includes GPU acceleration and advanced features, such as adaptive mesh refinement (AMR) and local adaptive time-stepping.

We start with a BH of dimensionless spin $a = 0.9$ surrounded by an equilibrium hydrodynamic torus with a sub-Keplerian angular momentum profile, $\ell \propto r^{1/4}$, inner edge at $r_{\rm in} = 6 r_g$, density maximum at $r_{\rm max} = 13.792 r_g$, and outer edge at $r_{\rm out} = 4 \times 10^4 r_g$ (Chakrabarti 1985; De Villiers & Hawley 2003); $r_g = G M_{\rm BH}/c^2$ is
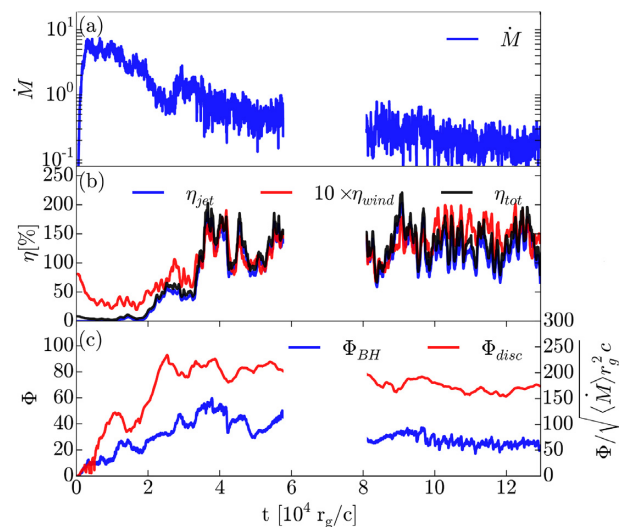

Figure 1. Time evolution of various quantities (data between $t = 5.7 \times 10^4$ and $t = 8.2 \times 10^4 r_g/c$ is missing). (a) The mass accretion rate $\dot{M}$ peaks at early times and gradually decreases; (b) The jets start out much weaker than the disc wind, $\eta_{\rm jet} \ll \eta_{\rm wind}$. However, the two become comparable at $t = (1.2–1.8) \times 10^4 r_g$, and at later times the situation reverses. Eventually, $\eta_{\rm jet}$ exceeds 100 per cent, i.e. jet power exceeds the accretion power. (c) This increase in jet power comes from the increase in the strength of BH poloidal magnetic flux, $\Phi_{\rm BH}$, due to the BH accreting dynamo-generated poloidal magnetic flux. Eventually, $\Phi_{\rm BH}$ exceeds a critical dimensionless value, $\Phi/(\langle \dot{M} \rangle r_g^2 c)^{1/2} \sim 50$, as seen from the right axis that shows the BH flux normalized by the late-time value of $\langle \dot{M} \rangle \approx 0.2$: $\Phi_{\rm BH}$ becomes dynamically important and leads to a MAD. A reservoir of positive poloidal magnetic flux $\Phi_{\rm disc}$ remains in the disc and may reach the BH at later times.

the gravitational radius. The torus aspect ratio ranges from $h/r = 0.2$ at $r_{\rm max}$ to 0.5 at $r_{\rm out}$. We insert into the torus toroidal magnetic field with a uniform plasma $\beta = p_{\rm gas}/p_{\rm mag} = 5$ and add random 5 per cent-level perturbations to $p_{\rm gas}$ to seed the non-axisymmetric MRI.

Operating in spherical polar coordinates, with a logarithmically spaced r-grid and uniform θ- and ϕ-grids, we use transmissive boundary conditions (BCs) at the poles, $\sin \theta = 0$ (see the supplementary information [SI] in Liska et al. 2018), periodic BCs in the ϕ-direction, and absorbing BCs at the inner and outer radial boundaries, located just inside of the event horizon and at $r = 10^5 r_g$, respectively (thus, both radial boundaries are causally disconnected from the accretion flow). We use a resolution of $N_r \times N_\theta \times N_\phi = 1872 \times 624 \times 1024$, resulting in a total of 1 billion cells. This results in 70–90 cells per disc scale height, $h/r \approx 0.35$–0.45. Such high resolutions are typically reserved for local shearing box simulations. To increase the time-step and maintain a near-unity cell aspect ratio everywhere, we reduce the ϕ-resolution near the pole (at $\sin \theta < 0.5$, using 4 AMR levels, from $N_\phi = 1024$ at equator to $N_\phi = 128$ at the poles; see also Liska et al. 2019a). We carry the simulation out to $t_{\rm F} \approx 1.3 \times 10^5 r_g/c$.

3 RESULTS

Fig. 1(a) shows that after peaking, mass accretion rate remains approximately constant at $t \lesssim 10^4 r_g/c$. At this time, the only outflow present is a sub-relativistic wind with energy efficiency $\eta_{\rm wind} \approx 5$ per cent (Fig. 1b). Poloidal magnetic flux on the BH, $\Phi_{\rm BH} = 0.5 \int_{r=r_{\rm H}} |B^r| \, {\rm d}A_{\theta\phi}$, grows from 0 to 20, as shown by the blue line (Fig. 1c). Here, the integral is over both hemispheres of the event
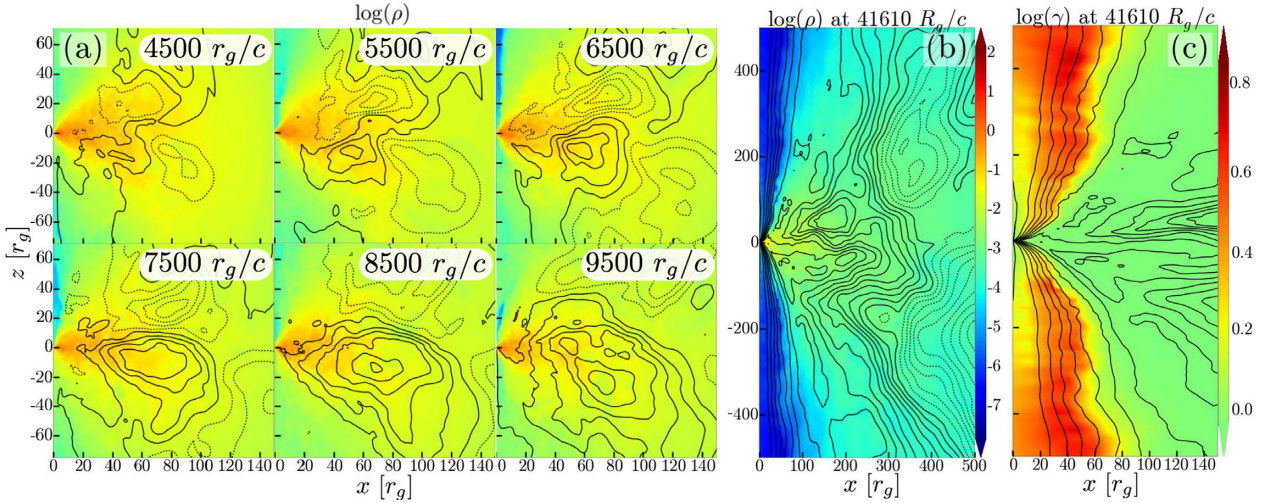
Figure 2. (a) Meridional slices through the simulation at the approximate times shown, illustrating the development of large-scale poloidal flux loops (black lines) of size comparable to the disc thickness, plotted over the density distribution (shown in colour; see the colour bar in panel b). The loops form slightly offset from the equator and buoyantly rise away from it, as expected in an $\alpha - \Omega$ dynamo. Initially, several poloidal field loops of positive (solid lines) and negative (dotted lines) polarity stochastically form. However, most of them get expelled, and one largest, lucky, loop takes over. See SI and this link for a movie. (b) A snapshot at $t = 4.2 \times 10^4 r_g/c$ reveals two large-scale dynamo-generated poloidal magnetic flux loops: their size, $l \gtrsim 100 r_g$, vastly exceeds that of the event horizon, and the loops present themselves to the BH as large-scale poloidal flux. (c) The colour map of the Lorentz factor, γ, shows that this flux leads to the launching of relativistic jets with a typical spine-sheath structure. The movie (see SI) shows no obvious signs of global kink or pinch modes in the jets, which reach $\gamma \sim 5$ at $z \lesssim 500 r_g$. We see no signs of such modes out to $z \sim 2000 r_g$ by which the jets reach $\gamma \sim 10$ (not shown due to space constraints).

horizon, $r_H = r_g[1 + (1 - a^2)^{1/2}]$, and the factor of 0.5 converts it to one hemisphere (Tchekhovskoy et al. 2011). The reservoir of positive poloidal magnetic flux in the disc, $\Phi_{\text{disc}} = \max_r \Phi_p(r)$ with $\Phi_p(r) = \max_\theta \int_0^\theta B^r dA_{\theta\phi}$, shown with the red line, also keeps growing, pointing to a large-scale dynamo activity in the disc. Here, $\max_r$ and $\max_\theta$ refer to the maxima taken over r and θ coordinates, respectively.

Fig. 2(a) shows a time sequence illustrating the generation of poloidal magnetic flux loops by the MHD turbulence (see the movie in the SI): several loops form just outside the equatorial plane, grow in strength, and buoyantly rise away from the equator. This process is stochastic: one of the loops ends up taking over the inner $100 r_g$ of the disc with the others getting expelled in outflows. This is consistent with the $\alpha - \Omega$ large-scale poloidal magnetic flux dynamo (Parker 1955; Moffatt 1978): a toroidal magnetic field loop undergoes Parker instability, buoyantly rises, and the Coriolis force twists it into a poloidal magnetic field loop. This way, the α-effect can convert toroidal into poloidal flux. The Ω-effect then does the opposite, shearing out this freshly generated poloidal magnetic flux loop into toroidal magnetic flux, and thereby completing the positive feedback cycle. This is a possible mechanism for both the initial formation of the poloidal magnetic flux loops and their subsequent runaway growth in strength and size, as seen here.

This picture is consistent with the butterfly diagram in Fig. 3: patches of toroidal magnetic field, b^ϕ, rise with alternating signs away from the equator. However, our dynamo is rather sporadic and irregular, reminiscent of lower plasma β (e.g. Bai & Stone 2013; Salvesen et al. 2016a) and sub-Keplerian (Nauman & Blackman 2015) shearing box simulations, and global simulations of very thick discs (Hogg & Reynolds 2018; Dhang & Sharma 2019) that show similar irregularity and even complete absence of sign flips. Global simulations at high β tend to show a more regular butterfly diagram (Shi, Krolik & Hirose 2010; Beckwith, Armitage & Simon 2011; O'Neill et al. 2011; Simon, Hawley & Beckwith 2011; Flock
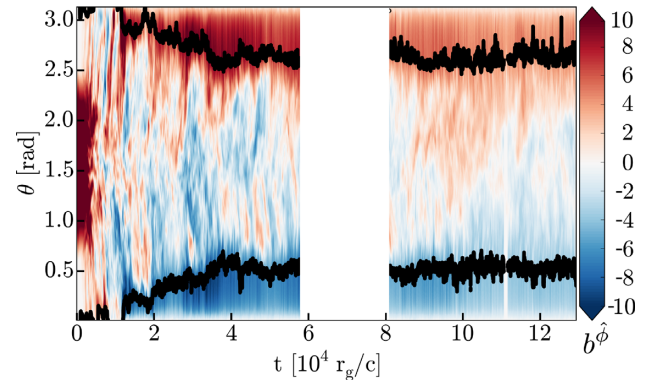

Figure 3. The space–time diagram of toroidally averaged rest-frame magnetic field b^ϕ at $r = 40 r_g$ shows an irregular butterfly pattern, indicating sporadic dynamo activity characteristic of thick, sub-Keplerian, or strongly magnetized discs (see Section 3). The black lines track the disc-jet boundary.

et al. 2012; Simon et al. 2012; Jiang, Stone & Davis 2017; Siegel & Metzger 2018).

Fig. 1(c), right axis, shows that the magnetic flux grows until the critical value $\Phi/(\langle \dot{M} \rangle r_g^2 c)^{1/2} \approx 50$ (Tchekhovskoy et al. 2011) at which the BH flux becomes dynamically important, obstructs accretion, and leads to a MAD. Fig. 1(b) shows that jets reach $\eta_{\text{jet}} \approx 150$ per cent, comparable to or exceeding 100 per cent: a tell-tale signature of the MAD state. Figs 4(a) and (b) shows that the jets collimate to small aspect ratios, $R/z \approx 0.3, 0.12, 0.08$, and accelerate to relativistic Lorentz factors, $\gamma \sim 3, 5, 10$ at $z/r_g = 100, 500, 2000$, respectively, similar to the observed M87 galaxy jet (see Appendix A; Nakamura & Asada 2013; Mertens et al. 2016; see also Chatterjee et al. 2019). During this process the jet converts magnetic energy into kinetic energy and heat, while the total mass and energy fluxes remain conserved, as seen in Fig. 4.
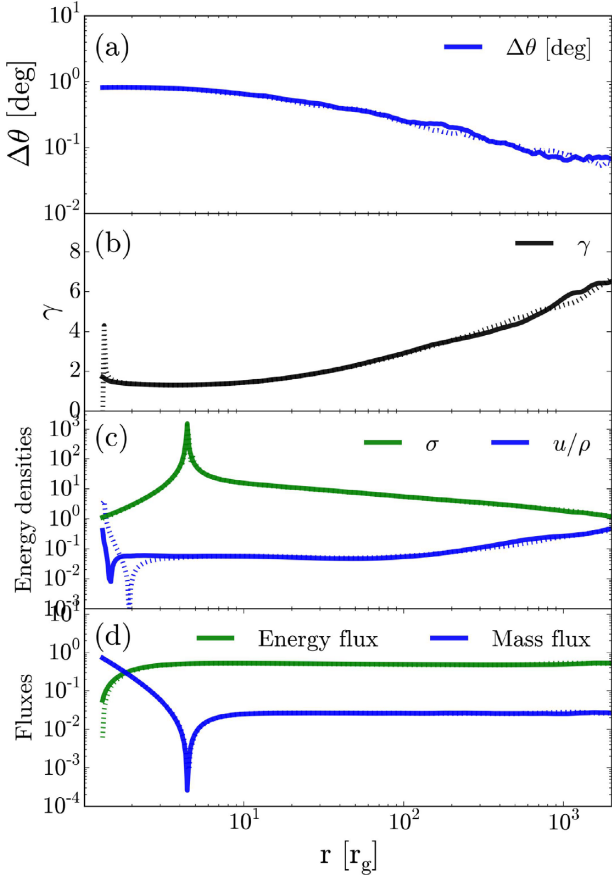
Figure 4. Radial profiles of the upper (dashed line) and lower (solid line) jet at $t = 3.75 \times 10^4 r_g/c$ averaged over $\Delta t = 5 \times 10^3 r_g/c$. (a) The half opening angle of the jet ($\Delta\theta$) decreases as the jet is collimated by the disc wind. (b) The jet readily accelerates to $\gamma \sim 6$ (weighted by the energy flux) over $2000 r_g$. Parts of the jet reach higher Lorentz factors (see Fig. A1). (c) As the jet accelerates the magnetization ($\sigma = b^2/\rho$) drops. Part of this magnetic energy is converted into kinetic energy and part of it heats up the jet leading to a rise in the specific internal energy (u/ρ). (d) The mass and energy fluxes integrated over the jet's opening angle remain (almost perfectly) conserved over $1000 r_g$.

Fig. 5(a) shows that whereas at early times the magnetic pressure in the disc is mostly subdominant, at later times it comes close to equipartition as characteristic of MADs (McKinney et al. 2012). This leads to relatively high α-viscosity in the disc, with Maxwell and Reynolds stress contributions of $\alpha_M = b_{\hat{r}} b_{\hat{\phi}}/(p_g + p_b) \simeq 0.1$ and $\alpha_R = \rho u_{\hat{r}} u_{\hat{\phi}}/(p_g + p_b) \simeq 0.01$, respectively; here the hats indicate the physical components. Such high Maxwell stresses are atypical and were only found in the presence of large-scale poloidal magnetic flux threading the disc (McKinney et al. 2012; Bai & Stone 2013; Salvesen et al. 2016a): indeed, while 40 per cent of the poloidal magnetic flux reaches the BH, the disc retains the rest; see Figs 2(b) and (c) and 5(c). If such *in situ* generation of equipartition ($\beta \sim 1$) magnetic fields from sub-equipartition toroidal fields carries over to thin discs, this may stabilize them against the viscous-thermal instability (Begelman & Pringle 2007; see also Sądowski 2016; Jiang et al. 2019). Interestingly, our recent simulation of a thin disc (with $h/r = 0.02$) initially threaded with a purely toroidal magnetic flux, did not show any signs of relativistic jets (Liska et al. 2019a). This suggests that the large-scale poloidal magnetic flux generation proceeds more efficiently for thick discs than for their thin counterparts.
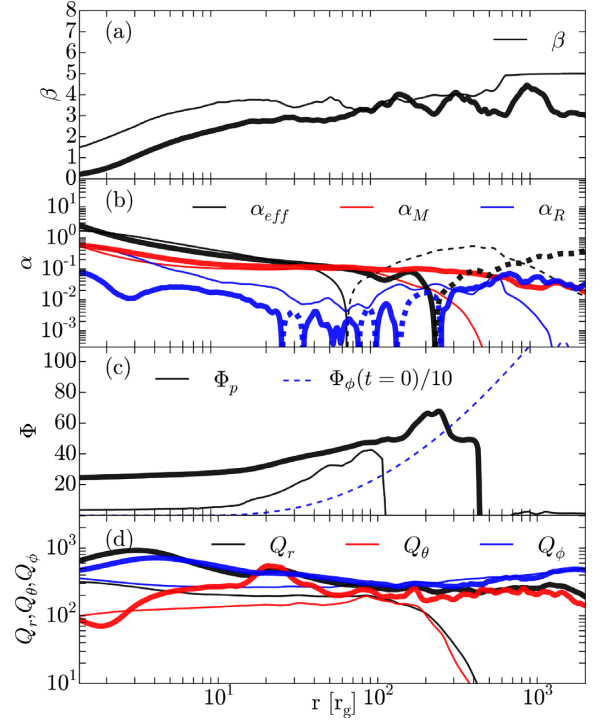
Figure 5. Radial profiles at $t = 10^4 r_g/c$ (thin lines) and $t = 1.3 \times 10^5 r_g/c$ (thick lines), averaged over $\Delta t = 10^3 r_g/c$. (a) While at early times the magnetic pressure is subdominant ($\beta \sim$ few), at late times the magnetic pressure reaches equipartition ($\beta \lesssim 1$), as the dynamo-generated poloidal magnetic flux increases in strength. (b) The effective viscosity, $\alpha_{\rm eff} = -v_{\hat{r}} v_{\hat{\phi}}/c_s^2$, and the contributions to viscosity of Maxwell (α_M) and Reynolds (α_R) stresses. The solid curves show positive and dashed negative values. Maxwell stress dominates over Reynolds stress. Near the BH we have $\alpha_{\rm eff} > \alpha_M$, likely due to plunging of the gas into the BH. Stagnation points in the flow, where $\alpha_{\rm eff} = 0$, are favourable locations for dynamo operation (see Section 4). (c) The disc has a large reservoir of positive polarity magnetic flux Φ_p, whose peak moves outward with time. The blue dashed line shows that the initial toroidal magnetic flux $\Phi_\phi(t = 0)$ (scaled by 0.1x) exceeds by a factor of ~ 7 the late-time poloidal flux at $200 r_g$, suggesting that even more poloidal magnetic flux may be generated at times beyond those simulated. (d) High values of quality factors, $Q_{\#}$, the number of cells per MRI wavelength in direction #, show that the turbulence is very well resolved in all three dimensions.

4 DISCUSSION AND CONCLUSIONS

Using global GRMHD simulations at one of the highest resolutions to date, we demonstrate for the first time that a large-scale poloidal magnetic flux dynamo operates in BH accretion discs. Poloidal field loops form *in situ*, of size $l \lesssim h \sim r$, slightly offset from the equator, and tend to rise buoyantly (Fig. 2a). The formation mechanism is consistent with the $\alpha - \Omega$ dynamo, which relies on the buoyancy and Coriolis forces to convert toroidal into poloidal magnetic flux (α-effect), and on the disc shear to convert poloidal into toroidal flux (Ω-effect). With most of the loops expelled, the lucky remaining loop structure resides at $r \gtrsim 200 r_g$ (Fig. 2b). It presents itself to the BH as a *large-scale poloidal magnetic flux*, whose scale exceeds the local radius by 2 orders of magnitude. The flux accumulates around the BH until it becomes dynamically important, and leads to a MAD and magnetically launched jets of constant magnetic polarity whose power exceeds the accretion power (Fig. 1b).

With the grid totalling 1 billion cells and effective resolution of $N_r \times N_\theta \times N_\phi = 1872 \times 624 \times 1024$ cells, this is the highest

resolution simulation of MADs. The much increased resolution – an increase in the number of cells by factors of approximately 200 compared to Tchekhovskoy et al. (2011) and 60 compared to White, Stone & Quataert (2019) – allows us to check whether the properties of MADs are sensitive to the changes in the resolution. We note that this unusually high resolution is combined with the extremely long duration of $t_F \approx 1.3 \times 10^5 r_g/c$, which allows us to ensure that the values of efficiency and magnetic flux have reached their asymptotic values and the simulation is firmly in the MAD regime. The time-average values of efficiency, $\eta_{tot} \approx 150$ per cent (Fig. 1b), and dimensionless magnetic flux, $\phi_{BH} \approx 50$ (Fig. 1c), are in agreement with previous findings for MADs at this thickness ($h/r \sim 0.35$–0.45). This suggests that the time-average results are numerically converged. Note that MADs are typically simulated by starting with initial conditions that contain a large amount of poloidal magnetic flux. In contrast, in this work, we started with a purely toroidal magnetic flux. That we find quantitatively similar results suggests that so long as the system ends up in a MAD state, the outcome is not sensitive to the path the system took to get there or the exact initial conditions it started with.

We initialized our simulations with a relatively strong toroidal magnetic field, with plasma $\beta = 5$, to ensure that they resolve the MRI due to both the initial toroidal and dynamo-generated poloidal magnetic fields: we found that the dynamo did not operate in the simulations that formally resolved the former but not the latter. Fig. 5(d) shows that the MRI is well-resolved, with $Q_{r,\theta} \gtrsim 100$ cells per MRI wavelength in the r-, and θ- and $Q_\phi \gtrsim 200$ in the ϕ-direction. Using the same physical setup, same effective θ-resolution near the equator, and four times lower ϕ-resolution, resulted in twice as low outflow energy efficiency of $\eta_{tot} \simeq 25$ per cent at $t = 2.5 \times 10^4 r_g/c$ (obtained with the HARM code at a resolution of $288 \times 128 \times 128$, with the θ-grid focused on the equator and using a toroidal wedge, $\Delta\phi = \pi$; see Appendix B). This suggests that for the toroidal flux to generate large-scale poloidal flux it is crucial that the MHD turbulence is well-resolved.

Fig. 5(c) shows that the poloidal flux produced in our simulation makes up $\lesssim 15$ per cent of the initial toroidal flux, $\Phi_p(r) = \int_0^r B^\phi dA_{r\theta}$, at $r \lesssim 200 r_g$; here, the integral is in the r- and θ-directions spanning the full range of $\theta \in [0, \pi]$. Thus, large-scale toroidal flux might be a prerequisite for the large-scale poloidal flux dynamo to operate. Assuming that the dynamo converts a fixed fraction of the initial toroidal flux into poloidal flux, it will take longer to generate the same poloidal flux for a weaker initial toroidal flux or, equivalently, higher value of plasma β. If the dynamo-generated poloidal magnetic flux is limited by the time available for the dynamo to operate, stagnation points in the disc – where the gas lingers instead of falling in or flying out and where the effective viscosity $\alpha_{eff} = -v_{\hat{r}} v_{\hat{\phi}}/c_s^2$ vanishes – can become centres of poloidal flux generation. Fig. 5(b) shows that the radius of the stagnation point changes very slowly: from $65 r_g$ at $t = 10^4 r_g/c$ to $230 r_g$ at $t = 1.3 \times 10^5 r_g/c$. The gas flow is directed away from the stagnation point in all directions, and this expanding flow pattern assists the dynamo not only in inflating the poloidal flux loop but also in trapping it at the stagnation point. As seen in Fig. 2(a), this trapping might be responsible for one lucky loop getting pinned down at the stagnation point, outgrowing the rest of the loops, and dominating the long-term evolution of the system. In a similar way, even for an initial small-scale toroidal magnetic field, a stagnation point may trap a poloidal magnetic flux loop and inflate it to large scales, thereby producing large-scale poloidal magnetic flux. Fig. 5(c) shows that in our simulations the peak of the poloidal flux grows in amplitude and moves out to a larger distance, loosely following the movement of the stagnation point. This suggests that the dynamo might indeed benefit from the presence of stagnation points in the flow. Since the stagnation point in externally fed accretion discs in XRBs and AGN would form around the disc's circularization radius located order(s) of magnitude further away from the BH than in this work, the buildup of poloidal flux on the BH would take much longer than presented in this work.

The lack of large-scale poloidal flux generation in global toroidal field GRMHD simulations till now might stem from a lower field strength considered, lack of stagnation points suitably located in the flow, a limited radial range of the initial toroidal magnetic flux distribution (Beckwith et al. 2008) or a high radial inflow velocity (due to large disc thickness) that may not give the poloidal field loops enough time to grow (McKinney et al. 2012). In addition, our work seems consistent with Fragile & Sadowski (2017), which for a strong $\beta \sim 0.1$ magnetic field did not find any generation of large-scale poloidal magnetic flux loops on a rather short time-scale of $\sim 1500 r_g/c$. It will be important to assess which (if any) of these speculations is correct. After we posted this work on the archives, Christie et al. (2019) showed in a toroidal-field simulation of a compact, neutrino-cooled merger remnant accretion disc that dynamo can generate *and* retain magnetic flux loops of alternating polarity, leading to striped jets (see also Parfrey, Giannios & Beloborodov 2015). The difference with our work can potentially emerge due to neutrino cooling and/or smaller disc size making their accretion flow more tightly bound and conducive to retaining the alternating-polarity dynamo-generated loops instead of expelling most of them in an outflow, as seen in Fig. 2(a).

A robust large-scale poloidal flux dynamo can help us understand the prevalence of jets across a wide range of astrophysical systems. Even though typical jet-producing accretion discs are thick near the BH, they may be thin at large radii (Esin, McClintock & Narayan 1997). Thin discs are thought to be incapable of efficiently transporting large-scale poloidal magnetic flux from the ambient medium to the BH (Lubow et al. 1994; Guilet & Ogilvie 2012, 2013), decreasing the prospects for jet formation. However, if the outer thin disc can transport even just a very weak poloidal magnetic flux, dynamo action in the inner, thick disc could amplify the magnetic flux *in situ* to levels sufficient for forming jets. In systems such as the jetted TDE Swift J1644+57 the stellar magnetic flux falls several orders of magnitude short of that necessary to power the observed jet (Kelley, Tchekhovskoy & Narayan 2014; Tchekhovskoy et al. 2014). The rapid dynamo action in this work may amplify the available magnetic flux, explaining their observed jet power.

REFERENCES

Bai X.-N., Stone J. M., 2013, ApJ, 767, 30
Balbus S. A., Hawley J. F., 1991, ApJ, 376, 214
Beckwith K., Hawley J. F., Krolik J. H., 2008, ApJ, 678, 1180
Beckwith K., Armitage P. J., Simon J. B., 2011, MNRAS, 416, 361
Begelman M. C., Pringle J. E., 2007, MNRAS, 375, 1070
Bhat P., Ebrahimi F., Blackman E. G., 2016, MNRAS, 462, 818
Blandford R. D., Znajek R. L., 1977, MNRAS, 179, 433
Brandenburg A., Nordlund A., Stein R. F., Torkelsson U., 1995, ApJ, 446, 741
Bromberg O., Tchekhovskoy A., 2016, MNRAS, 456, 1739
Chakrabarti S. K., 1985, ApJ, 288, 1
Chatterjee K., Liska M., Tchekhovskoy A., Markoff S. B., 2019, MNRAS, 490, 2200
Christie I. M., Lalakos A., Tchekhovskoy A., Fernández R., Foucart F., Quataert E., Kasen D., 2019, MNRAS, 490, 4811
Colella P., Woodward P. R., 1984, J. Comput. Phys., 54, 174
Davis S. W., Stone J. M., Pessah M. E., 2010, ApJ, 713, 52
De Villiers J.-P., Hawley J. F., 2003, ApJ, 589, 458
Dhang P., Sharma P., 2019, MNRAS, 482, 848
Esin A. A., McClintock J. E., Narayan R., 1997, ApJ, 489, 865
Fabian A. C., 2012, ARA&A, 50, 455
Flock M., Dzyurkevich N., Klahr H., Turner N., Henning T., 2012, ApJ, 744, 144
Fragile P. C., Sadowski A., 2017, MNRAS, 467, 1838
Gammie C. F., McKinney J. C., Tóth G., 2003, ApJ, 589, 444
Ghisellini G., Tavecchio F., Maraschi L., Celotti A., Sbarrato T., 2014, Nature, 515, 376
Guilet J., Ogilvie G. I., 2012, MNRAS, 424, 2097
Guilet J., Ogilvie G. I., 2013, MNRAS, 430, 822
Hawley J. F., Krolik J. H., 2006, ApJ, 641, 103
Hogg J. D., Reynolds C. S., 2018, ApJ, 861, 24
Jiang Y.-F., Stone J., Davis S. W., 2019, ApJ, 880, 67
Jiang Y.-F., Blaes O., Stone J., Davis S. W., 2019, ApJ, 885, 144
Kelley L. Z., Tchekhovskoy A., Narayan R., 2014, MNRAS, 445, 3919
Komissarov S. S., 2001, MNRAS, 326, L41
Lesur G., Ogilvie G. I., 2008, A&A, 488, 451
Liska M. et al., 2019a, preprint (arXiv:1912.10192)
Liska M., Hesp C., Tchekhovskoy A., Ingram A., van der Klis M., Markoff S., 2018, MNRAS, 474, L81
Liska M., Tchekhovskoy A., Ingram A., van der Klis M., 2019b, MNRAS, 487, 550
Lubow S. H., Papaloizou J. C. B., Pringle J. E., 1994, MNRAS, 267, 235
McKinney J. C., 2006, MNRAS, 368, 1561
McKinney J. C., Tchekhovskoy A., Blandford R. D., 2012, MNRAS, 423, 3083
Mertens F., Lobanov A. P., Walker R. C., Hardee P. E., 2016, A&A, 595, A54
Moffatt H. K., 1978, in Wilders J., ed., Magnetic Field Generation in Electrically Conducting Fluids. Cambridge University Press, Cambridge, England, p. 353
Nakamura M., Asada K., 2013, ApJ, 775, 118
Narayan R., Sądowski A., Penna R. F., Kulkarni A. K., 2012, MNRAS, 426, 3241
Nauman F., Blackman E. G., 2015, MNRAS, 446, 2102
Narayan R., Igumenshchev I. V., Abramowicz M. A., 2003, PASJ, 55, L69

Nemmen R. S., Tchekhovskoy A., 2015, MNRAS, 449, 316
Noble S. C., Krolik J. H., Hawley J. F., 2009, ApJ, 692, 411
O'Neill S. M., Reynolds C. S., Miller M. C., Sorathia K. A., 2011, ApJ, 736, 107
Parfrey K., Giannios D., Beloborodov A. M., 2015, MNRAS, 446, L61
Parker E. N., 1955, ApJ, 122, 293
Penna R. F., McKinney J. C., Narayan R., Tchekhovskoy A., Shafee R., McClintock J. E., 2010, MNRAS, 408, 752
Pessah M. E., Chan C.-k., Psaltis D., 2007, ApJ, 668, L51
Prieto M. A., Fernández-Ontiveros J. A., Markoff S., Espada D., González-Martín O., 2016, MNRAS, 457, 3801
Ressler S. M., Tchekhovskoy A., Quataert E., Gammie C. F., 2017, MNRAS, 467, 3604
Rothstein D. M., Lovelace R. V. E., 2008, ApJ, 677, 1221
Ryan B. R., Gammie C. F., Fromang S., Kestener P., 2017, ApJ, 840, 6
Salvesen G., Simon J. B., Armitage P. J., Begelman M. C., 2016a, MNRAS, 457, 857
Salvesen G., Armitage P. J., Simon J. B., Begelman M. C., 2016b, MNRAS, 460, 3488
Shafee R., McKinney J. C., Narayan R., Tchekhovskoy A., Gammie C. F., McClintock J. E., 2008, ApJ, 687, L25
Shi J., Krolik J. H., Hirose S., 2010, ApJ, 708, 1716
Shi J.-M., Stone J. M., Huang C. X., 2016, MNRAS, 456, 2273
Siegel D. M., Metzger B. D., 2018, ApJ, 858, 52
Simon J. B., Hawley J. F., Beckwith K., 2011, ApJ, 730, 94
Simon J. B., Beckwith K., Armitage P. J., 2012, MNRAS, 422, 2685
Stone J. M., Hawley J. F., Gammie C. F., Balbus S. A., 1996, ApJ, 463, 656
Sądowski A., 2016, MNRAS, 459, 4397
Tchekhovskoy A., Bromberg O., 2016, MNRAS, 461, L46
Tchekhovskoy A., McKinney J. C., 2012, MNRAS, 423, L55
Tchekhovskoy A., McKinney J. C., Narayan R., 2008, MNRAS, 388, 551
Tchekhovskoy A., Narayan R., McKinney J. C., 2010, ApJ, 711, 50
Tchekhovskoy A., Narayan R., McKinney J. C., 2011, MNRAS, 418, L79
Tchekhovskoy A., Metzger B. D., Giannios D., Kelley L. Z., 2014, MNRAS, 437, 2744
White C. J., Stone J. M., Quataert E., 2019, ApJ, 874, 168

SUPPORTING INFORMATION

Supplementary data are available at *MNRAS* online.

Generation of a strong poloidal magnetic field around a rapidly spinning black hole V2.mp4

Please note: Oxford University Press is not responsible for the content or functionality of any supporting materials supplied by the authors. Any queries (other than missing material) should be directed to the corresponding author for the article.

APPENDIX A: LARGE-SCALE JET PROPERTIES

Fig. A1 shows a vertical slice through the Lorentz factor of one of our jets. The jets have a fast sheath and a slow spine (see also Tchekhovskoy, McKinney & Narayan 2008). While the jets are not axisymmetric, they remain largely stable and accelerate to Lorentz factors of $\gamma \sim 10$ at distances of $z = 2000r_g$.
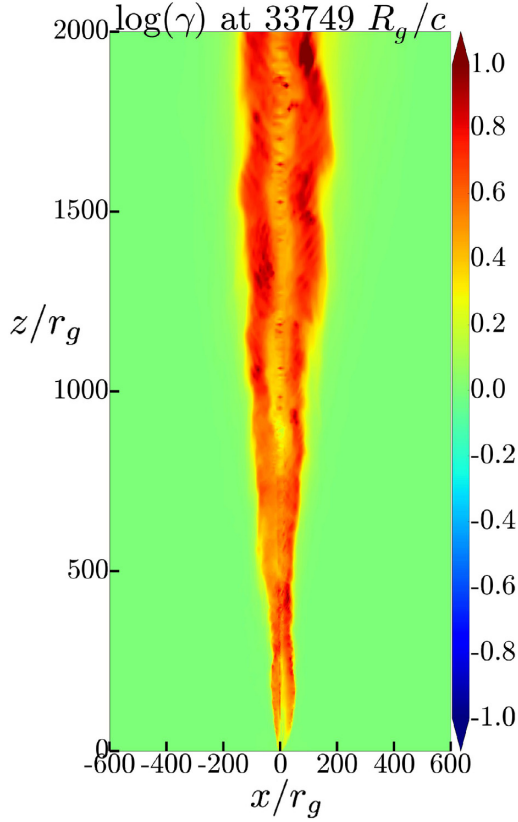
Figure A1. Vertical slice through the Lorentz factor in a simulation snapshot of the upper relativistic jet extending out to $r = 2000 r_g$. While the jets show deviations from axisymmetry, they do not undergo significant kink of pinch instabilities and reach Lorentz factors of $\gamma \sim 10$. As the jets accelerate, they collimate into progressively smaller opening angles, which become as small as $\theta \sim 0.08$ (see also Fig. 4).

APPENDIX B: DESCRIPTION OF THE LOW-RESOLUTION HARM SIMULATION

We can glean the effect of changing numerical resolution on the large-scale poloidal magnetic flux dynamo by comparing to a lower-resolution HARM simulation that showed the signs of large-scale poloidal magnetic flux dynamo for the first time. We carried it out using the HARM code at a resolution of $288 \times 128 \times 128$, with the θ-grid focused on the equator at small distances while at the same time collimating towards the polar regions to resolve the jets at large distances (see Tchekhovskoy et al. 2011; Ressler et al. 2017). This simulation used a reduced toroidal wedge of $\Delta\phi = \pi$, with

periodic boundary conditions in φ. The focusing of the numerical grid towards the equatorial plane results in grid cell aspect ratio near the equatorial plane of $\Delta r : r\Delta\theta : r\Delta\phi \approx 3 : 1 : 4$, i.e. cells elongated in radial and toroidal directions. Fig. B1 shows the time-dependence of mass accretion rate, jet efficiency, and magnetic flux versus time. As you can see, by $t \sim 30,000 r_g/c$, the HARM simulation reaches outflow energy efficiency of $\eta \sim 25$ per cent, about half of that in the H-AMR simulation. This suggests that large-scale poloidal magnetic flux dynamo is more vigorous at a higher resolution, full azimuthal extent of the grid, and/or near-unity aspect ratio of the cells within the accretion disc. We will determine the factors important for resolving the dynamo activity in future work.
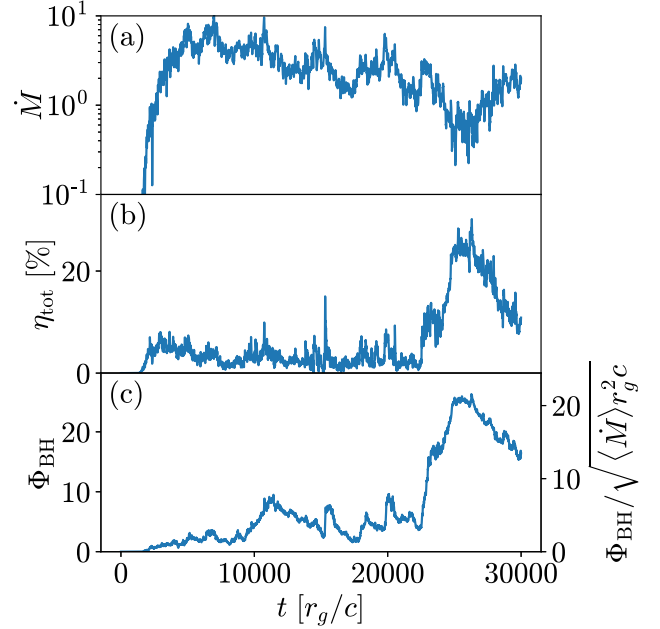
Figure B1. Similar to Fig. 1 but for our low-resolution HARM simulation. While [panel (a)] the mass accretion rate shows a qualitatively similar behaviour – peak around $\dot{M} \approx 6$ before declining – as for our fiducial run, [panel (b)] the outflow energy efficiency reaches $\eta_{tot} \simeq 25$ per cent for this lower-resolution run, twice as low as for the fiducial model over the same time interval (see Fig. 1b), and [panel (c)] the magnetic flux reaches $\Phi_{BH} \approx 25$, also remains approximately twice as small as for the fiducial model (see Fig. 1c). The magnetic flux normalized to the late-time-average mass accretion rate ($\langle\dot{M}\rangle \approx 1.5$) reaches $\simeq 20$ (right axis in panel (c)).

This paper has been typeset from a TeX/LaTeX file prepared by the author.